Supplemental information for: Tunnelling of transverse acoustic waves on a silicon chip

Nicolas P. Mauranyapin,* Erick Romero,* Rachpon Kalra, Glen Harris, Christopher G. Baker, and Warwick P. Bowen

ARC Centre for Engineered Quantum Systems, School of Mathematics and Physics,
The University of Queensland, Brisbane, Queensland 4072, Australia

I. SPRING COUPLING

Instead of evanescent coupling, as used in this paper, coupling between mechanical systems can be achieved with spring coupling via direct real phonons as used when connecting resonators with free suspended beams (see figure 1 (a) and (b)) [1–3]. These two techniques are however quite different. Indeed, as described in the theoretical section of the main text, in the tunnelling coupling case, the acoustic wave vector is imaginary in the barrier but is real in the case of spring coupling (see figure 1 (c)) which is exactly what distinguishes transfers via real and virtual phonons. For this reason, at specific frequencies or beam lengths the acoustic wave may resonate in the free beam, which is not the case for evanescent coupling since the wave decays exponentially along the barrier. The coupling rate between two resonators connected via a free beam will be influenced by the resonances of the beam as shown in figure 1 (d) which oblige to rely on an off-resonance situation of the coupler [4]. This greatly reduces the ability to control the coupling strength compared to an evanescent barrier leading to a reduction of the system's bandwidth of operation and fabrication tolerances. In addition energy up to 50% of the total energy of the mechanical system can be captured by the free beam coupler. By contrast, only 0.03% of the energy is stored in the coupler in the case of evanescent coupling as displayed in figure 1 (e) showing that the energy mostly stays distributed in the resonators when coupled with tunnelling.

MEMS and sensing applications ranging from clocks, memories, spin detection [5], inertial [6] and mass sensing [7] benefit from high-Q resonators which require large isolation from the environment and very low controllable coupling rates. Such configuration can be challenging to fabricate with spring coupling, as it would require either free suspended beams much longer than the resonator itself or very narrow coupling beams. Indeed, as shown in figure 1 (d), the coupling rate achievable with a 1.2 mm long coupler can be three orders of magnitude lower using tunnelling coupling instead of spring coupling (0.2 Hz compared to 500 Hz). In addition, according to our simulations, a coupling rate of 100 Hz can be achieved with a tunnel barrier of ~ 350 μm (see figure 1 (d)) but necessitate a free beam longer than 4 cm (data not shown), increasing the device foot print by two orders of magni-

---

* These authors contributed equally to this work

tude for this example. In addition, because the coupling rate scales exponentially in the case of tunnelling, we expect that this foot print reduction will greatly increase when lower coupling rate are needed to be achieved.

A. Mode filtering

We demonstrated in the main text mode filtering using evanescent coupling. Since spring coupling is fundamentally different, one can wonder if filtering can also be achieved with real phonons. This is possible by leveraging the symmetry of the spring modes and waveguides mode but adds complexity to the device. Let's consider the configuration where the coupling spring is attached to the middle (in the transverse direction) of the input and output waveguide (as shown between the two square membranes of figure 1 (a)). In this configuration, the spatial overlap between a symmetric spring mode and antisymmetric input or output modes is zero and vice versa. Consequently, when the input waveguide is excited at a frequency where the first two modes can propagate, if a symmetric transverse spring mode is used to couple the two waveguides, only the first mode will be transmitted resulting in mode filtering. The opposite is true when an antisymmetric spring mode is used leading to filtering of the fundamental guide mode.

Compared to mode filtering using tunnelling, this has again the disadvantage of been frequency dependant since symmetric and antisymmetric spring modes will have different frequencies. Moreover, the efficiency of the filter can not be tuned by changing the length of the coupler as for tunnelling. Instead, the coupler can be fabricated off-centred in the transverse direction to increasing the overlap between symmetric and antisymmetric modes. This strategy allows tuning of the coupling into both modes using a spring coupler but is more complex to predict than evanescent coupling as knowledge of the three modes shapes is needed.

II. INFLUENCE OF THE MESH ON THE WAVE PROPAGATION

To determine the influence of the mesh on the propagation of the acoustic wave, we use finite element simulations. We simulated an infinite waveguide actuated by acoustic waves with wavevectors k_y including the range of wavevectors used in the main text. The frequency of the wave is then calculated to determine the dispersion
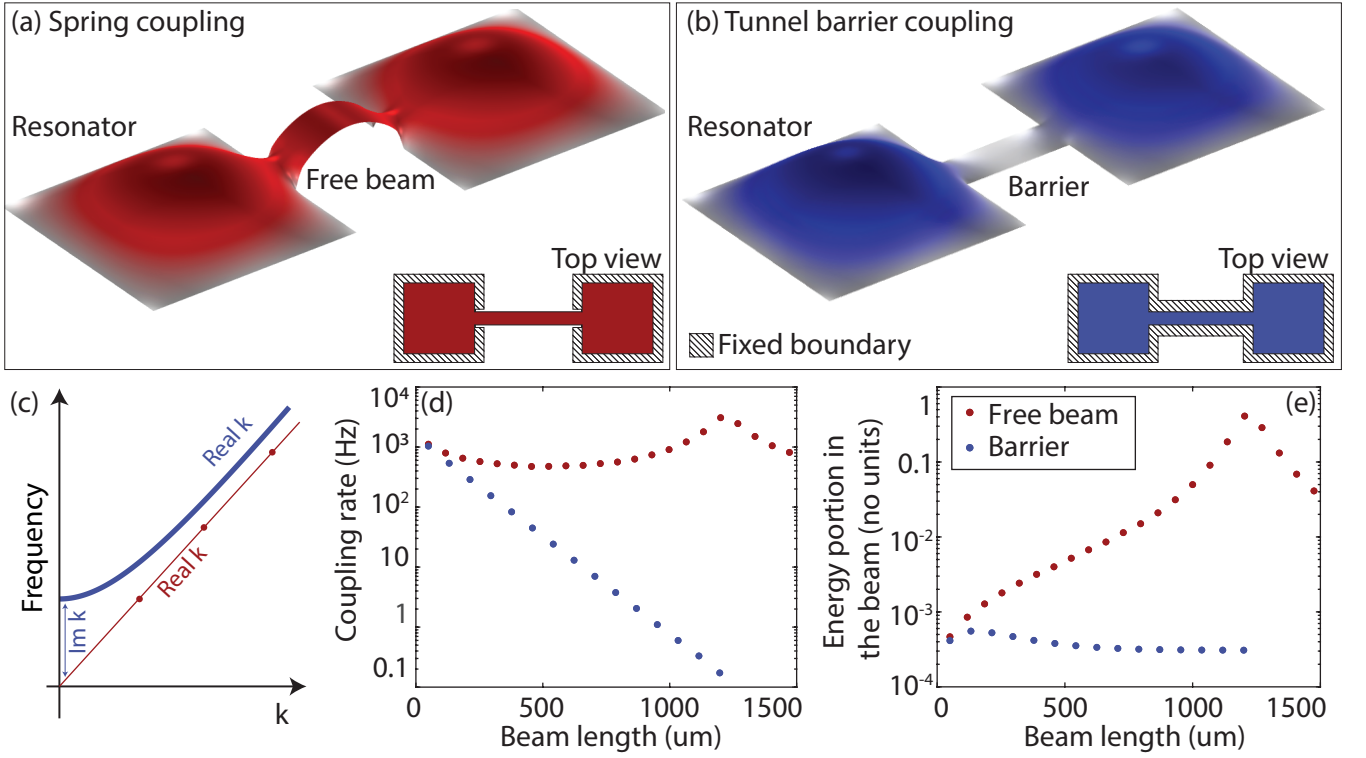
Figure 1. Mechanical coupling simulations. (a) Two square membranes (2 mm×2 mm) mechanical resonators coupled via a free beam. (b) Two mechanical resonators coupled via a tunnel barrier. The insets in (a) and (b) represent the top view of the devices. (c) Dispersion relation of the coupling element of the tunnel barrier (blue) and the free beam (red). The resonances of the free beam are represented by the dots along the red line. (d) Coupling rate between the two resonators as function of the length of the coupling element for both cases. (e) Energy stored in the coupling element normalised to the total energy as function of the length of the coupling element for both cases.

relation of the waveguide. As shown in figure 2, this simulation is performed on waveguides without mesh (top diagram) and with meshes of three different hole sizes (remaining diagrams). The finer pattern correspond to a mesh with holes of 1 μm as used in our device presented in the main text. The second pattern from the bottom corresponds to a mesh with hole size of 9 μm and the bottom pattern to hole size of 26 μm. Clear perturbation of the propagation can be seen on the dispersion relation of the waveguide with the 26 μm holes (blue trace) similar to what is observed in phononic crystals [8]. However, the dispersion relation of the 9 μm hole mesh (red trace) follows the trend of the dispersion relation of the non-patterned membrane (purple trace) and the 1 μm hole mesh (yellow trace) is in even closer agreement. Simulations of the dispersion relation of waveguides with even finer meshes (not shown here) do not converge towards the dispersion relation of the non-patterned waveguide and maintain similar dispersion relations to that of the 1 μm hole mesh. This behaviour is expected because the mesh modifies both the density ρ and the stress σ of the membrane (see Appendix A of the main text) resulting in a change in the wave velocity $v = \sqrt{\sigma/\rho}$ and an offset in the dispersion relation compared to a non-patterned membrane (see Eq. 1 of the main text).

To determine this offset, we used simulation to compare the resonance frequencies of a squared membrane with and without a 1 μm hole meshed and we find a reduction of the resonance frequencies by a factor of 0.9 when the mesh is present. Since these resonance frequencies are proportional to v we concluded that the wave velocity in a meshed waveguide is reduced by 0.9. This was further verified experimentally in figure 3. In this figure, we compare the observed resonance frequencies of a waveguide (red trace) with corrected wave velocity theoretical predictions (grey trace). One can clearly see that the corrected predictions are in excellent agreement with the experimental data.

We thus concluded that the meshed does not perturb the propagation of acoustic waves for the range of frequencies/wave vector used in the experiment of the main text. The behaviour of our waveguides can then be predicted accurately by the dispersion relation of a non-patterned waveguide with a wave velocity reduced by a factor 0.9.
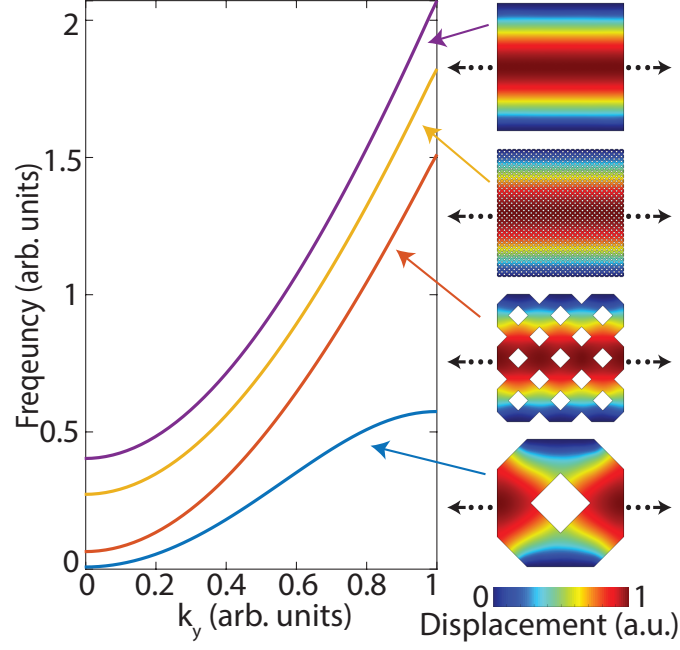
Figure 2. Simulated dispersion for different mesh sizes. The purple curve corresponds to the dispersion relation of a infinite non-patterned waveguide. The yellow, red and blue curves correspond to a infinite waveguide patterned with 1 μm, 9 μm and 26 μm holes mesh respectively. The unitary cell repeated to construct each infinite waveguides is shown on the right where the colors represent the displacement created by an acoustic wave of infinite wavelength (k=0). Note that the bottom unitary cell is an example of unitary cell used to create the mesh.
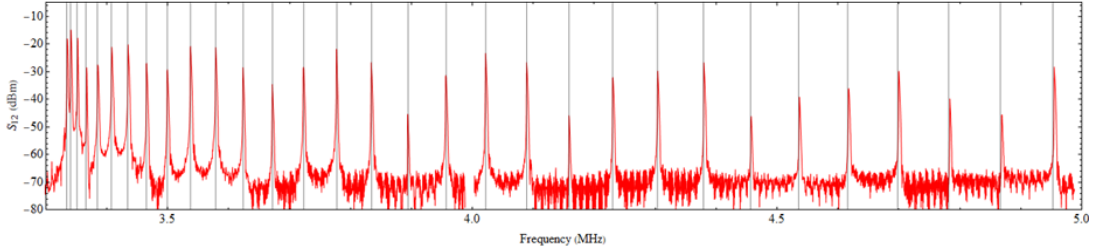

Figure 3. Network analysis compared with theoretical predictions. The red trace represents the experimental network response of a meshed waveguide excited at different frequencies and exhibits resonances. These resonance frequencies are compared with theoretical predictions with a wave velocity corrected by a factor 0.9 (grey traces).

III. MECHANICAL NONLINEARITIES

Setting aside the intrinsic material nonlinearities, arising from the higher order corrections to the material's stiffness tensor, the main source of mechanical nonlinearities are *geometric* nonlinearities, arising due to surface and area changes brought about from the eigenmode deformation. In order to illustrate the different role played by geometric nonlinearities, we consider the flexural and longitudinal modes of a beam resonator in figure 4. For the case of out-of-plane motion of a doubly-clamped beam (or string), the geometric nonlinearity leads the linear spring term $k\,x$ to be supplemented by an additional nonlinear restoring force αx^3 with $\alpha > 0$, arising from the extra tensioning of the beam due to its elonga-

tion for large excursions from equilibrium [9]. This is the classic Duffing nonlinearity, leading to an additional stiffening of the resonators confining potential $\frac{\alpha}{4}x^4$, as shown by the green dashed line in figure 4 (c), and an amplitude-dependent increase the resonator's eigenfrequency. In the case of longitudinal motion (figure 4 (b)), the geometric nonlinearity arises from changes in the cross-sectional area of the beam. However, in contrast to the case of out-of-plane motion—where stiffening occurred in both up and down directions— here the stiffening is followed by softening during a mechanical oscillation, as the beam's cross-section is successively enlarged and reduced. This leads to a different nonlinear restoring force of the type βx^2, leading to a correction to the trapping potential of the form $\frac{\beta}{3}x^3$, as illustrated by the dashed orange curve

in figure 4 (c). The net effect of such a nonlinearity is only a modest spring softening, which can be absorbed into an effective correction to the Duffing nonlinearity [10, 11]. For this type of motion, the geometric nonlinearity is sufficiently weak that strong nonlinearities are typically only achieved, in the case of silicon, by reaching the material's intrinsic nonlinearities, at much higher energy densities [9, 12].

IV. NANOMECHANICAL MASS SENSING

Nanomechanical resonators have been widely demonstrated as a tool to measure mass with exquisite precision, even down to yoctogram [13]. The principle of operation is that a deposited particle of mass Δm changes the resonance frequency Ω of the mechanical resonator by increasing its mass from m to $m + \Delta m$ without altering its spring constant $k = m\Omega^2$. Then the shifted frequency $\Omega' = \sqrt{k/(m + \Delta m)} \approx \Omega(1 - \Delta m/2m)$ for $\Delta m \ll m$. We see then that the frequency shift is $\Delta\Omega/\Omega = -\Delta m/2m$ motivating the use of a low mass mechanical oscillator.

Two methods to resolve the frequency shifts have proved highly effective in the literature [14]: 1-feedback can be introduced to cause the mechanical resonator to regeneratively oscillate, greatly increasing the precision with which a frequency shift can be observed; 2-the mechanical resonator can be driven on resonance with an external sinusoidal drive force in a phase locked loop configuration, with the phase shift providing a precise measure of the resonance frequency. Either way, it has been shown that the minimum resolvable mass change is approximately [14, 15]

$$\delta m \approx 2m \left(\frac{E_{th}}{E_n}\right)^{1/2} \left(\frac{\Delta f}{Q\Omega}\right)^{1/2}, \qquad (1)$$

where $E_{th} = k_B T$ is the thermal energy in the resonator, with T its temperature and k_B Boltzmann's constant, E_n is the energy of the coherent oscillation after regenerative amplification or coherent driving, and Δf is the measurement bandwidth in Hertz (all other frequencies are angular).

Without loss of generality, we consider henceforth the case of coherent driving, using a phase locked loop for readout. The expression above can be written in terms of the amplitude of the applied force F on the resonator and its frequency Ω by recognising that $E_n = kx^2/2$, where x is the amplitude of mechanical oscillation, and that for resonant driving $x = FQ/m\Omega^2$ [16]. We then find

$$\delta m = \sqrt{8k_B T\Delta f} \times \frac{1}{F}\left(\frac{m^3\Omega}{Q^3}\right)^{1/2}. \qquad (2)$$

This shows that for fixed temperature and drive force, the sensitivity improves with increasing Q and decreasing m and Ω. Given that, for a given mass, out-of-plane acoustic waves generally have significantly lower

frequency than compressional waves, this suggests that mass sensing should be more effective using out-of-plane motion. The ability to increase the Q of out-of-plane modes by introducing tensile stress can further be expected to provide an advantage for out-of-plane modes.

To put this on a rigorous footing, we consider a resonator that is rectangular with dimensions (length, width, thickness) = (l, w, t). Compressional and out-of-plane modes in such a geometry have closely similar effective masses, therefore we take the masses to be equal. We also assume that the drive force, measurement bandwidth, and temperature are the same, to ensure a fair comparison. The ratio of the mass sensing performance is then

$$\frac{\delta m_{\text{comp}}}{\delta m_{\text{strg}}} = \left(\frac{\Omega_{\text{comp}}}{\Omega_{\text{strg}}}\right)^{1/2} \times \left(\frac{Q_{\text{strg}}}{Q_{\text{comp}}}\right)^{3/2}. \qquad (3)$$

1. Mode frequencies

The compressional modes have frequency [17]

$$\Omega_{\text{comp}} = \frac{n\pi}{l}\sqrt{\frac{E}{\rho}}, \qquad (4)$$

where n is the mode number, E is Young's modulus and ρ is the density of the medium; while out-of-plane string modes have frequency [17]

$$\Omega_{\text{strg}} = \frac{n\pi}{l}\sqrt{\frac{E}{\rho}}\left(\frac{1}{12}\left(\frac{\pi n t}{l}\right)^2 + \frac{\sigma}{E}\right)^{1/2}, \qquad (5)$$

where σ is the tensile stress of the string. We see then that the ratio of resonance frequencies is

$$\frac{\Omega_{\text{comp}}}{\Omega_{\text{strg}}} = \left(\frac{1}{12}\left(\frac{\pi n t}{l}\right)^2 + \frac{\sigma}{E}\right)^{-1/2}. \qquad (6)$$

Taking the highly stressed limit for out-of-plane modes, where the σ term dominates, we can simplify this expression to

$$\frac{\Omega_{\text{comp}}}{\Omega_{\text{strg}}} = \sqrt{\frac{E}{\sigma}}. \qquad (7)$$

2. Quality factor

Compared to a compressional mode, an out-of-plane mode under tension experiences a dilution of its dissipation, boosting its quality factor above the intrinsic material limit $Q_{\text{intrinsic}}$. Indeed, the quality factor of a string under tensile stress is [17]

$$Q_{\text{strg}} = \left(\frac{1}{12}\left(\frac{n\pi t}{l}\right)^2 \frac{E}{\sigma} + \frac{1}{\sqrt{3}}\left(\frac{t}{l}\right)\sqrt{\frac{E}{\sigma}}\right)^{-1} Q_{\text{intrinsic}}. \qquad (8)$$
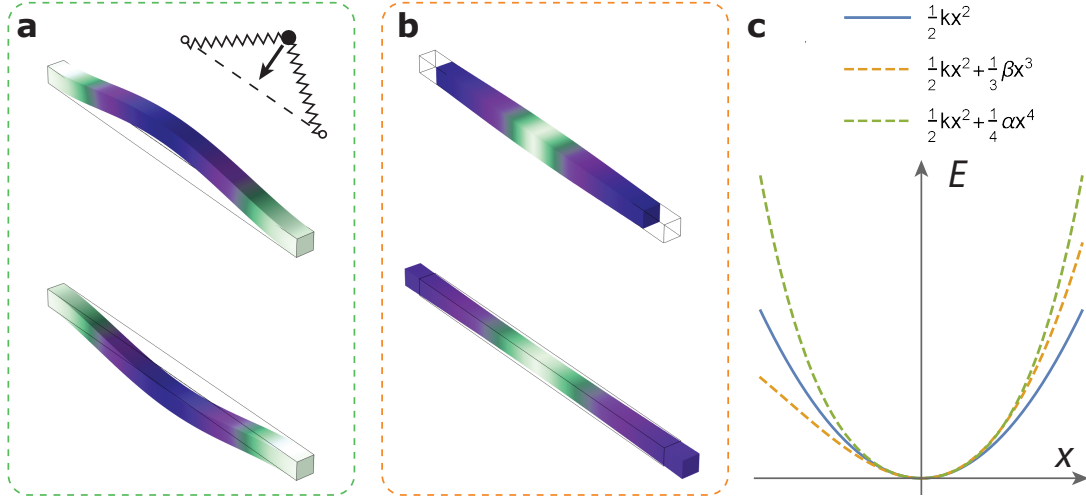
Figure 4. Mechanical nonlinearities. (a) Out-of-plane motion of a beam resonator, showing the deflection extrema, with inset illustrating the origin of the Duffing nonlinearity. (b) Longitudinal eigenmode of the beam. (c) Effect of nonlinearities on the confining potential E.

Note, here that the quality factor increases as the aspect ratio l/t increases.

To enable a simple comparison, we assume that the intrinsic quality factor is the same for compressional and out-of-plane modes, we then find a quality factor enhancement

$$\frac{Q_{\text{strg}}}{Q_{\text{comp}}} = \left(\frac{1}{12} \left(\frac{n\pi t}{l} \right)^2 \frac{E}{\sigma} + \frac{1}{\sqrt{3}} \left(\frac{t}{l} \right) \sqrt{\frac{E}{\sigma}} \right)^{-1}. \quad (9)$$

To obtain a simple dependence, we take the appropriate limit of a high aspect ratio (l/t large) so that the first term under the square-root can be neglected. We then find

$$\left(\frac{Q_{\text{strg}}}{Q_{\text{comp}}} \right)_{\text{large aspect ratio}} = \sqrt{3} \left(\frac{l}{t} \right) \sqrt{\frac{\sigma}{E}}. \quad (10)$$

3. Comparison of mass sensing performance

Combining the Ω and Q dependence, we find the ratio of resolvable masses

$$\left(\frac{\delta m_{\text{comp}}}{\delta m_{\text{strg}}} \right)_{\sigma \text{ large}} = 3^{3/4} \left(\frac{l}{t} \right)^{3/2} \left(\frac{\sigma}{E} \right)^{1/2}. \quad (11)$$

Since $E/\sigma \sim 200$, but $(l/t) \sim 10^3$ to 10^4, we see that – at least in the case where the dissipation is limited by intrinsic dissipation (which is now routinely reached in many cases) – the performance of a string mode with high tensile stress can be expected to exceed that of a compressional mode by four to five orders of magnitude. We note that these conclusions depend on the assumption of a fixed drive force. This is an appropriate assumption in many cases, since it can be challenging to strongly drive nanomechanical devices. An alternative assumption that could be taken is that the amplitude of mechanical motion is limited by appearance of nonlinearities in the dynamics, and that the drive force is sufficient to reach this regime. It has recently been shown that different conclusions can be drawn under this assumption [18].

[1] S. Lee and C.-C. Nguyen, "Mechanically-coupled micromechanical resonator arrays for improved phase noise," in *Proceedings of the 2004 IEEE International Frequency Control Symposium and Exposition, 2004.*, pp. 144–150, IEEE, 2004.
[2] M. U. Demirci and C. T.-C. Nguyen, "Mechanically corner-coupled square microresonator array for reduced series motional resistance," *Journal of Microelectromechanical Systems*, vol. 15, no. 6, pp. 1419–1436, 2006.
[3] D. S. Greywall and P. A. Busch, "Coupled micromechanical drumhead resonators with practical application as electromechanical bandpass filters," *Journal of Micromechanics and Microengineering*, vol. 12, no. 6, p. 925, 2002.
[4] K. Fang, M. H. Matheny, X. Luan, and O. Painter, "Optical transduction and routing of microwave phonons in cavity-optomechanical circuits," *Nature Photonics*, vol. 10, no. 7, pp. 489–496, 2016.

[5] J. Košata, O. Zilberberg, C. L. Degen, R. Chitra, and A. Eichler, "Spin detection via parametric frequency conversion in a membrane resonator," *Physical Review Applied*, vol. 14, no. 1, p. 014042, 2020.

[6] D. K. Shaeffer, "Mems inertial sensors: A tutorial overview," *IEEE Communications Magazine*, vol. 51, no. 4, pp. 100–109, 2013.

[7] S. Marquez, M. Álvarez, J. A. Plaza, L. Villanueva, C. Domínguez, and L. M. Lechuga, "Asymmetrically coupled resonators for mass sensing," *Applied physics letters*, vol. 111, no. 11, p. 113101, 2017.

[8] M. Kurosu, D. Hatanaka, K. Onomitsu, and H. Yamaguchi, "On-chip temporal focusing of elastic waves in a phononic crystal waveguide," *Nature communications*, vol. 9, no. 1, pp. 1–7, 2018.

[9] V. Kaajakari, T. Mattila, A. Oja, and H. Seppa, "Nonlinear limits for single-crystal silicon microresonators," *Journal of Microelectromechanical Systems*, vol. 13, pp. 715–724, Oct. 2004.

[10] R. Lifshitz and M. Cross, "Nonlinear dynamics of nanomechanical and micromechanical resonators," *Reviews of nonlinear dynamics and complexity*, vol. 1, pp. 1–52, 2008.

[11] Y. L. Sfendla, C. G. Baker, G. I. Harris, L. Tian, R. A. Harrison, and W. P. Bowen, "Extreme quantum nonlinearity in superfluid thin-film surface waves," *npj Quantum Information*, vol. 7, no. 1, pp. 1–12, 2021.

[12] V. Kaajakari, T. Mattila, A. Lipsanen, and A. Oja, "Nonlinear mechanical effects in silicon longitudinal mode beam resonators," *Sensors and Actuators A: Physical*, vol. 120, pp. 64–70, Apr. 2005.

[13] J. Chaste, A. Eichler, J. Moser, G. Ceballos, R. Rurali, and A. Bachtold, "A nanomechanical mass sensor with yoctogram resolution," *Nature nanotechnology*, vol. 7, no. 5, pp. 301–304, 2012.

[14] K. Ekinci, Y. Yang, and M. Roukes, "Ultimate limits to inertial mass sensing based upon nanoelectromechanical systems," *Journal of applied physics*, vol. 95, no. 5, pp. 2682–2689, 2004.

[15] M. A. Taylor, A. Szorkovszky, J. Knittel, K. H. Lee, T. G. McRae, and W. P. Bowen, "Cavity optoelectromechanical regenerative amplification," *Optics express*, vol. 20, no. 12, pp. 12742–12751, 2012.

[16] This relationship between x and F can be readily obtained by solving $m\ddot{x} + m(\Omega/Q)\dot{x} + kx = F \sin \Omega t$.

[17] S. Schmid, L. G. Villanueva, and M. L. Roukes, *Fundamentals of nanomechanical resonators*, vol. 49. Springer, 2016.

[18] S. K. Roy, V. T. Sauer, J. N. Westwood-Bachman, A. Venkatasubramanian, and W. K. Hiebert, "Improving mechanical sensor performance through larger damping," *Science*, vol. 360, no. 6394, 2018.